

Atomically synergistic Zn-Cr catalyst for iso-stoichiometric co-conversion of ethane and CO₂ to ethylene and CO

Received: 17 July 2023

Accepted: 9 January 2024

Published online: 30 January 2024

Check for updates

Ji Yang^{1,2,12}, Lu Wang^{3,12}, Jiawei Wan^{4,12}, Farid El Gabaly^{5,12}, Andre L. Fernandes Cauduro⁵, Bernice E. Mills⁵, Jeng-Lung Chen⁶, Liang-Ching Hsu⁷, Daewon Lee⁴, Xiao Zhao⁴, Haimei Zheng⁴, Miquel Salmeron⁴, Caiqi Wang⁸, Zhun Dong⁸, Hongfei Lin⁸, Gabor A. Somorjai⁹, Fabian Rosner¹⁰, Hanna Breunig¹⁰, David Prendergast², De-en Jiang^{3,11}✉, Seema Singh⁵✉ & Ji Su^{1,2}✉

Developing atomically synergistic bifunctional catalysts relies on the creation of colocalized active atoms to facilitate distinct elementary steps in catalytic cycles. Herein, we show that the atomically-synergistic binuclear-site catalyst (ABC) consisting of Zn^{δ+}-O-Cr⁶⁺ on zeolite SSZ-13 displays unique catalytic properties for iso-stoichiometric co-conversion of ethane and CO₂. Ethylene selectivity and utilization of converted CO₂ can reach 100 % and 99.0% under 500 °C at ethane conversion of 9.6%, respectively. In-situ/ex-situ spectroscopic studies and DFT calculations reveal atomic synergies between acidic Zn and redox Cr sites. Zn^{δ+} (0 < δ < 2) sites facilitate β-C-H bond cleavage in ethane and the formation of Zn-H^{δ-} hydride, thereby the enhanced basicity promotes CO₂ adsorption/activation and prevents ethane C-C bond scission. The redox Cr site accelerates CO₂ dissociation by replenishing lattice oxygen and facilitates H₂O formation/desorption. This study presents the advantages of the ABC concept, paving the way for the rational design of novel advanced catalysts.

The synergistic effects generated by mixed or supported bifunctional catalysts are often claimed to promote the catalytic performance of traditional heterogeneous catalysts^{1–9}. Recently, the construction of synergistic pair-sites with colocalized metal atoms to facilitate distinct elementary steps in the catalytic reaction has been established as a crucial step toward atomically synergistic bifunctional catalyst development^{10–12}. The interaction between these adjacent metal atoms,

similar to the metal-support interaction of traditional heterogeneous catalysts^{3,13}, offers the possibility to modulate their respective electronic structure to further enhance their catalytic activity^{11,14–17}. However, precisely controlling their colocalization requires a complicated synthesis process with multiple synthesis steps to load single atoms^{10,18}. Moreover, the stability of the well-defined synergistic sites is debatable, especially under harsh reaction conditions such as high

¹Energy Storage and Distributed Resources Division, Lawrence Berkeley National Laboratory, Berkeley, CA, USA. ²The Molecular Foundry, Lawrence Berkeley National Laboratory, Berkeley, CA, USA. ³Department of Chemistry, University of California, Riverside, CA, USA. ⁴Materials Sciences Division, Lawrence Berkeley National Laboratory, Berkeley, CA, USA. ⁵Sandia National Laboratories, Livermore, CA, USA. ⁶National Synchrotron Radiation Research Center, Science-Based Industrial Park, Hsinchu, Taiwan. ⁷Department of Soil and Environmental Sciences, National Chung Hsing University, Taichung, Taiwan. ⁸Gene and Linda Voiland School of Chemical Engineering and Bioengineering, Washington State University, Pullman, WA, USA. ⁹Department of Chemistry, University of California, Berkeley, CA, USA. ¹⁰Energy Analysis and Environmental Impacts Division, Lawrence Berkeley National Laboratory, Berkeley, CA, USA. ¹¹Department of Chemical and Biomolecular Engineering, Vanderbilt University, Nashville, TN, USA. ¹²These authors contributed equally: Ji Yang, Lu Wang, Jiawei Wan, Farid El Gabaly. ✉e-mail: de-en.jiang@vanderbilt.edu; seema.rose.singh@gmail.com; jisu@lbl.gov

reaction temperatures^{18,19}. The benefits and remaining challenges of atomically synergistic bifunctional catalysts motivate us to further explore new synthesis routes, new reaction applications, and their synergistic effects with the goals to accelerate the development of next-generation atomically synergistic catalysts.

Growing CO₂ emissions and abundant shale gas reserves have prompted a significant amount of research to explore efficient approaches for co-utilizing the products to produce value-added chemicals^{20–22}. Ethane, the second-largest component of shale gas, is an ideal alternative hydrogen source for CO₂ conversion. The co-conversion of ethane and CO₂ ($C_2H_6 + CO_2 \rightarrow C_2H_4 + CO + H_2O$) is a viable alternative to the ethane steam cracking for ethylene production under the goal of net negative CO₂ emissions²¹. Furthermore, iso-stoichiometric co-conversion of ethane and CO₂ (ICEC) to ethylene and CO is crucial for direct downstream processes such as the hydroformylation reaction to produce aldehyde²³ and polymerization process to produce polyketones^{24–27}. However, the ICEC process lacks a viable catalyst for achieving high ethylene selectivity and CO₂ utilization simultaneously. Metal-based catalysts suffer from the inevitable cleavage of C–C bonds through dry reforming pathways and lower the ethylene selectivity^{22,28–30}. Oxide-based catalysts exhibit the great merit of preferential C–H bond scission over C–C bond scission pathways but require excessive CO₂ cofeeding to reduce ethane adsorption and scavenge the surface H species^{31,32}. Specifically, Zn and Cr oxide-based catalysts were widely studied for co-conversion of ethane and CO₂. The acidic Zn²⁺ site displayed high activity for C–H bond cleavage in ethane and CO₂ activation, requiring the participation of adjacent active sites to form binuclear sites^{33–35}. The challenge is that acidified Zn²⁺–H hydride displays a capacity for C–C bond scission of ethane, leading to undesired production of methane. Redox Cr⁶⁺ sites require lattice oxygen as a H acceptor to dissociate C–H bonds but trigger the formation of less active Cr³⁺ species. The reoxidation of Cr³⁺ to Cr⁶⁺ is limited by slow O abstraction from CO₂²⁰. The above analyses thus indicate the need for the development of an atomically-synergistic binuclear Zn–O–Cr site catalyst for ICEC, with Zn facilitating CO₂ adsorption and activation to provide O species for Cr⁶⁺ regeneration and adjacent Cr as an electron donor reducing the acidity of Zn²⁺ to facilitate its activity and selectivity for C–H bond scission^{6,36–39}. More generally, exploring a cooperative redox and acid-base catalytic mechanism for ICEC is highly desirable.

In this work, we show the successful fabrication and demonstration of a Zn–O–Cr atomically-synergistic binuclear-site catalyst (ABC) that is highly efficient for ICEC with high ethylene selectivity and utilization of converted CO₂ (U_{CO₂}). As we will show, compared with pure Zn and Cr catalysts, Zn–O–Cr ABC displays -1.5 and -4-fold higher catalytic activity with 100% ethylene selectivity and 99.0% U_{CO₂} under optimized reaction conditions. Key to this high performance is the discovery that Cr facilitates the formation of a Zn^{δ+} ($0 < \delta < 2$) site to enhance the β–C–H bond cleavage of ethane, while the resulting Lewis base Zn–H^δ hydride favors CO₂ adsorption and activation, and prevents C–C bond scission of ethane. The redox Cr site accelerates CO₂ dissociation and facilitates H₂O formation/desorption. The apparent activation energies of ethane conversion and CO₂ conversion are -70.9 and -74.0 kJ/mol, which demonstrates the rate matching achieved in ICEC.

Results

Controlling Zn and Cr coordination structure

Catalysts were synthesized by mixing a constant total amount of zinc (II) acetate and chromium (III) acetate hydroxide on a SSZ-13 zeolite support with varying Zn/Cr molar ratios, followed by direct decomposition at 550°C and then Na⁺ neutralization of acidic site on supports (Fig. 1a). The catalyst synthesis method developed here will be referred to as the dry-deposition method (The experimental details are summarized in Methods). The catalysts are denoted as Zn_xCr_y/SSZ-13, where *x*/*y* refers to the ratio of Zn/Cr (*x*=1, *y*=0; *x*/*y*=1/2, 1, 2, 3, 4;

x=0, *y*=1). The textural properties, composition analysis, and surface acidity of SSZ-13 and synthesized catalysts are characterized by N₂ physisorption, X-ray fluorescence (XRF), and attenuated total reflection Fourier transform infrared (ATR-FTIR) measurements (Supplementary Figs. 1–2 and Tables 1–2). Transmission electron microscopy (TEM), scanning TEM (STEM) images, and energy dispersive spectroscopy (EDS) elemental mappings (Fig. 1b and Supplementary Figs. 3–5) demonstrate high dispersion of Zn and/or Cr oxide phases, with no observable sintering of oxide nanoparticles. The X-ray diffraction (XRD) results reveal the absence of spinel ZnCr₂O₄ and zincite ZnO for all dry-deposition synthesized catalysts. Cr₂O₃ phases with R3c space group were only observed in Cr/SSZ-13 and Zn₁Cr₂/SSZ-13 (Supplementary Fig. 6). The control samples with same amount Zn and Cr precursors were prepared via a co-precipitation method (CP), followed by Na⁺ neutralization. ZnCrO_x nanoparticles are observed in CP-synthesized samples (Supplementary Fig. 7). And a phase transition from spinel ZnCr₂O₄ to ZnO (Supplementary Fig. 8) was detected on CP-synthesized catalysts with Zn/Cr ratios varying from 1/2 to 3/1^{40–42}.

Figure 1c, Supplementary Figs. 9–11 and Supplementary Table 3 show X-ray photoelectron spectroscopy (XPS) results for Zn 2*p*, Zn LMM Auger and Cr 2*p*_{3/2} spectra. The formation of Zn^{δ+} ($0 < \delta < 2$) was confirmed through Auger spectra of Zn LMM. The subpeaks at 987.5 and 990.0 eV in Auger spectra of Zn LMM (Supplementary Fig. 10) are assigned to the Zn²⁺ and Zn^{δ+} ($0 < \delta < 2$), respectively⁴³. And the subpeaks at -576 and -580 eV in Cr 2*p*_{3/2} XPS (Supplementary Fig. 11) were assigned to the Cr³⁺ and Cr⁶⁺, correspondingly⁴⁴. Figure 1c shows the proportion of Zn^{δ+} ($0 < \delta < 2$) and Cr⁶⁺ relative to the total amount of (Zn^{δ+} + Zn²⁺) and (Cr⁶⁺+Cr³⁺) in Zn_xCr_y/SSZ-13 catalysts, respectively. These proportions vary with Zn/Cr ratios, with the highest Zn^{δ+} ($0 < \delta < 2$) proportion generated at Zn/Cr ratio of 3/1 and the highest Cr⁶⁺ proportions produced at Zn/Cr ratios of 3/1 and 4/1. We hypothesize that the proximal electronic interactions between Zn and Cr could modify their respective oxidation states. This is consistent with the Zn L₃-edge X-ray absorption near-edge structure (XANES) spectra analyses (Supplementary Fig. 12), which suggests a decrease in the oxidation state of Zn in Zn_xCr_y/SSZ-13 samples compared to pure Zn/SSZ-13 sample. The Zn^{δ+} and Cr⁶⁺ content in the CP-synthesized Zn₃Cr₁/SSZ-13 sample is similar to those of pure Zn/SSZ-13 and Cr-SSZ-13 samples, respectively (Supplementary Fig. 13).

XANES spectra (Fig. 1d and Supplementary Fig. 14) and extended X-ray absorption fine structure (EXAFS) spectra (Fig. 1e, f, Supplementary Figs. 15–18, Supplementary Tables 4–5) were used to study coordination structures of Zn and Cr sites. As shown in Fig. 1d and Supplementary Fig. 14, the electron transition from Zn 1s to Zn 4*p* unoccupied orbitals (Feature A) is revealed in Zn K-edge XANES spectra; and Cr K-edge XANES spectra exhibits the peak of electron transition from Cr 1s to Cr 3*d*-O 2*p* unoccupied orbitals (Feature B). As the Zn/Cr ratio increases from 1/1 to 4/1 in Zn_xCr_y/SSZ-13 catalysts, the intensity of feature A decreases, suggesting electron occupation in Zn 4*p* unoccupied orbitals, while the intensity of feature B increases, which suggests electrons transfer out of Cr 3*d*-O 2*p* orbitals near the conduction band minimum. We hypothesize a link between these observations, that electronic charge transfers from Cr 3*d*-O 2*p* character in the conduction band to Zn 4*p*^{45,46}, due to a strong Zn–Cr interaction. Thus, the charge transfer decreases the oxidative state of Zn²⁺ to Zn^{δ+} ($0 < \delta < 2$), which is consistent with XPS and Auger results (Fig. 1c). In Fig. 1e, the scattering peaks at 1.50 Å are assigned to Zn–O coordination in the first shell. The pure Zn/SSZ-13 and Zn_xCr_y/SSZ-13 samples exhibited a significantly lower intensity for this Zn–O scattering peak than the ZnO reference, suggesting a higher degree of crystal disorder^{47,48}. The scattering peaks at -2.85 Å are assigned to Zn–O–Zn coordination in the second shell. Compared to Zn/SSZ-13 and the ZnO reference, Zn₁Cr₁/SSZ-13 and Zn₃Cr₁/SSZ-13 exhibited no peak for Zn–O–Zn coordination. Instead, a new peak at -3.08 Å should be attributed to the Zn–O–Cr bond⁴¹. Differently, Zn₄Cr₁/SSZ-13 sample has both Zn–O–Cr and Zn–O–Zn bonds. Cr

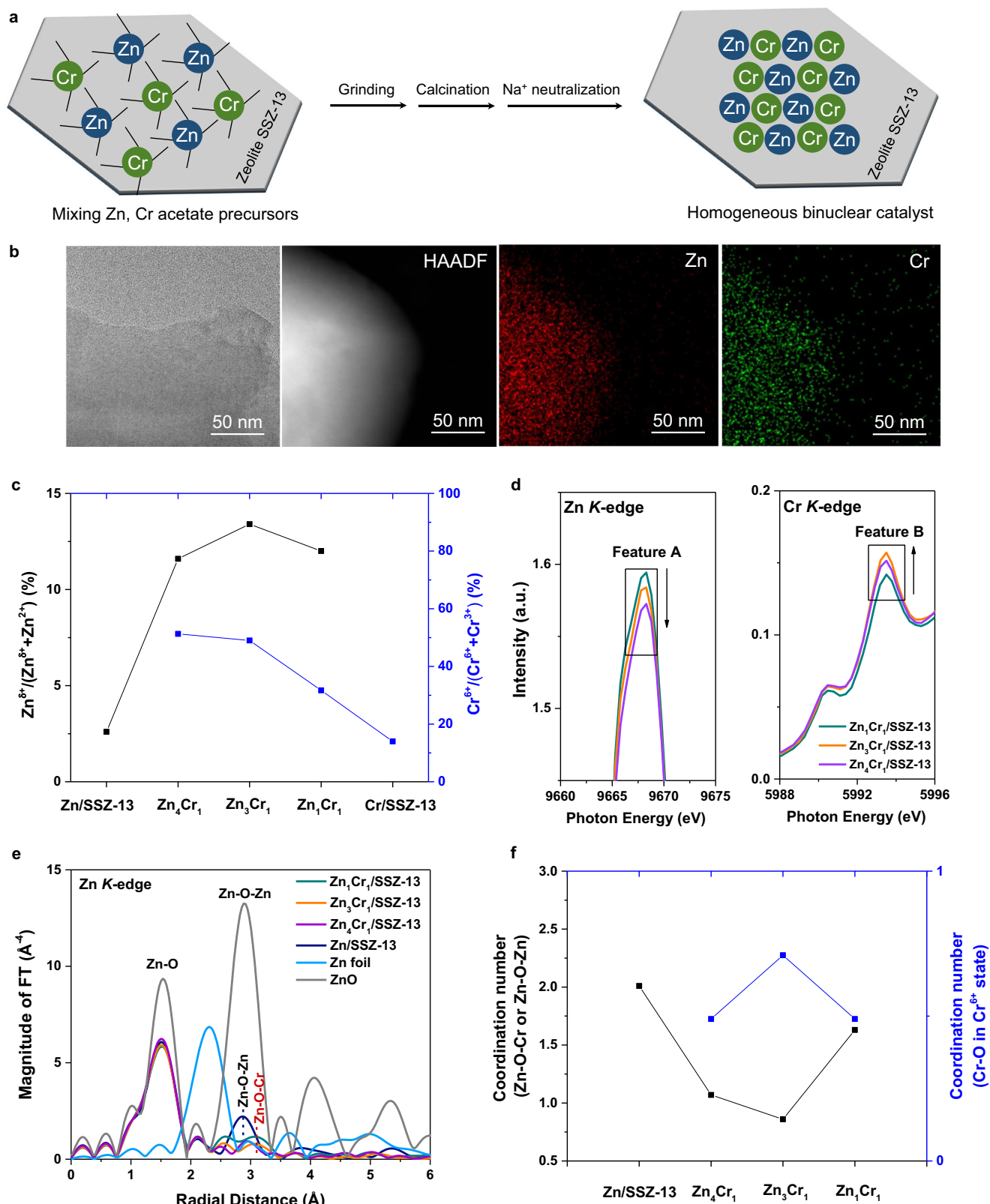


Fig. 1 | Coordination of Zn-O-Cr sites in atomically-synergistic binuclear-site catalyst (ABC). **a** Schematic illustration of the fabrication process of Zn-O-Cr ABC. **b** Representative TEM and HAADF-STEM images and EDS mapping of Zn-O-Cr ABC with Zn/Cr ratio of 3/1; **c** The proportion of Zn^{δ+} ($0 < \delta < 2$) (left) and Cr⁶⁺ (right) with varying Zn/Cr ratios (Results derived from Auger spectra of Zn LMM and Cr

2p_{3/2} XPS spectra); **d** Enlarged electron transition features in Zn and Cr K-edge XANES spectra; **e** k³-weighted Fourier-transformed extended X-ray absorption fine structure (FT-EXAFS) spectra (Zn K-edge) of Zn-O-Cr ABCs with varying Zn/Cr ratios, with Zn foil and ZnO as references; **f** Coordination number (CN) of Zn-O-Cr(Zn) and Cr-O in Cr⁶⁺ state in Zn-O-Cr ABCs with varying Zn/Cr ratios.

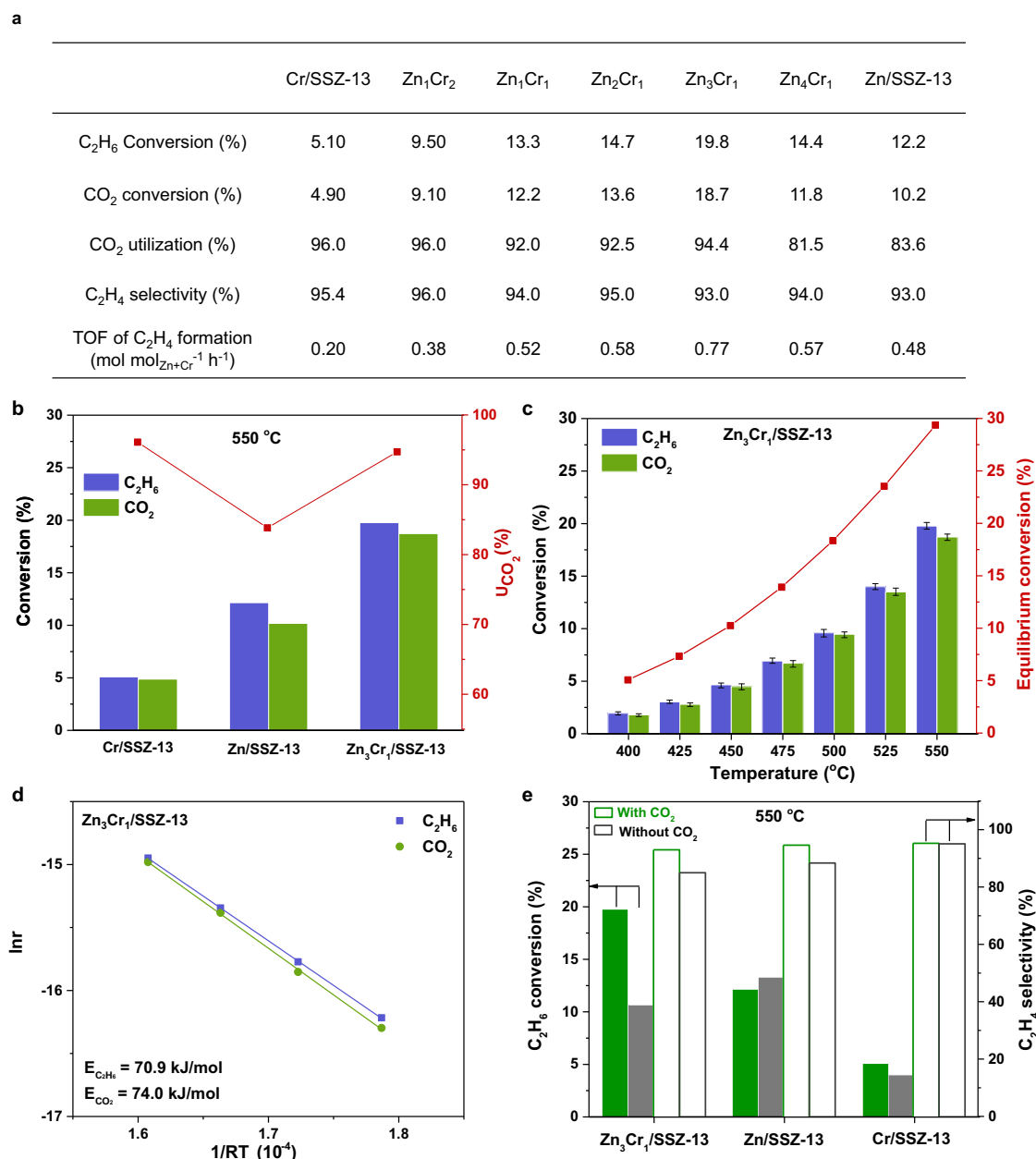


Fig. 2 | Iso-stoichiometric co-conversion of ethane and CO₂ (ICEC). **a** Catalytic performance of Zn-O-Cr ABCs (Reaction condition: Temperature = 550 °C; Reactant composition = 5% C₂H₆ + 5% CO₂ + 90% Ar; WHSV = 7500 mL g⁻¹ cat h⁻¹); **b** C₂H₆ and CO₂ conversion, utilization of converted CO₂ (U_{CO₂}) of Cr/SSZ-13, Zn/SSZ-13, and Zn₃Cr₁/SSZ-13 catalysts in ICEC at 550 °C; **c** Reaction temperature dependent

performance of Zn₃Cr₁/SSZ-13 catalyst. **d** Arrhenius plots of Zn₃Cr₁/SSZ-13 catalyst (obtained when both C₂H₆ and CO₂ conversions are <10 %). **e** C₂H₆ conversion and C₂H₄ selectivity over Zn₃Cr₁/SSZ-13, Zn/SSZ-13, and Cr/SSZ-13 with (green columns) /without (gray columns) CO₂ at 550 °C.

K-edge Fourier transformed EXAFS (FT-EXAFS) spectra of Cr-containing samples (Supplementary Fig. 15) displayed Cr-O scattering peaks located at 1.51 Å, which is similar to standard peak of Cr-O scattering 1.50 Å in Cr^{III}O₃; but as Zn/Cr ratio increase to 3/1 and 4/1, a visible shoulder peak corresponding to standard peak of Cr-O scattering at 1.20 Å in K₂Cr^{VI}O₇ appeared, indicating that Zn₃Cr₁/SSZ-13 and Zn₄Cr₁/SSZ-13 samples have two types of Cr-O coordination. Supplementary Tables 4-5 show the EXAFS-derived fitting parameters. Zn_{*x*}Cr_{*y*}/SSZ-13 catalyst (*x*/*y* = 1, 3, 4) samples show Zn-O-Cr coordination with a bond distance -3.4 Å in phase-corrected space, which corresponds to the emergent peak at -3.08 Å in Fig. 1e⁴¹. These results provide solid evidence for the formation of a Zn^{δ+}-O-Cr⁶⁺ structure in Zn_{*x*}Cr_{*y*}/SSZ-13. Notice that Zn_{*x*}Cr_{*y*}/SSZ-13 samples also exhibited lower coordination numbers (CNs) for Zn-O and Zn-O-Cr compared to the pure Zn/SSZ-

13 sample (Fig. 1f and Supplementary Table 4), which results from Cr colocalization. Especially, for the Zn₃Cr₁/SSZ-13 and Zn₄Cr₁/SSZ-13 samples, the CNs of Zn-O and Zn-O-Cr are 3.94 and 0.86, and 3.77 and 1.07, respectively. And Zn₃Cr₁/SSZ-13 has the highest CN for the Cr-O bond in hexavalent (Cr⁶⁺) states. Therefore, these results confirm the formation of hetero binuclear Zn^{δ+}-O-Cr⁶⁺ sites, and Zn₃Cr₁/SSZ-13 exhibits the highest population of the Zn^{δ+}-O-Cr⁶⁺ site.

Catalytic performance of Zn-O-Cr ABC for ICEC

Figure 2a, b and Supplementary Fig. 19 and Table 6 show the ICEC catalytic performance of Zn-O-Cr ABCs under the reaction conditions of weight hourly space velocity (WHSV) of 7500 mL g⁻¹ cat h⁻¹ and a CO₂/ethane ratio of 1 at 550 °C. The Zn₃Cr₁/SSZ-13 ABC catalyst displayed the best performance among all tested catalysts, with the highest C₂H₆

conversion (19.8%), CO₂ conversion (18.7%), turnover frequency (TOF) of C₂H₄ formation (0.77 mol mol_{Zn+Cr}⁻¹ h⁻¹), as well as excellent C₂H₄ selectivity (93.0%) and U_{CO₂} (94.4%). Previous studies have mainly focused on achieving high ethane conversion and ethylene selectivity in co-conversion of ethane and CO₂ by co-feeding excess CO₂ at CO₂/ethane ratios of 2–6^{49–53}. In the ICEC process the C₂H₄ selectivity and U_{CO₂} are two important factors for evaluating the success of catalyst development. Utilization of converted CO₂ (U_{CO₂}) is defined as the ratio of CO₂ conversion to ethane conversion on an iso-stoichiometric basis. Compared with previous studies in Supplementary Table 7 and Fig. 21, the Zn₃Cr₁/SSZ-13 catalyst displays the highest space-time yield (STY) of C₂H₄ formation (0.086 kg h⁻¹ kg_{cat}⁻¹) and the highest U_{CO₂} at 550 °C, which clearly shows the superiority of Zn–O–Cr ABCs. Furthermore, Fig. 2c and Supplementary Table 7 show C₂H₄ selectivity can achieve 100% and U_{CO₂} is 99.0% under the reaction temperature of 500 °C, with ethane conversion of 9.6% and CO₂ conversion of 9.5%. These results further demonstrate the advantage of Zn–O–Cr ABCs suitable for ICEC. In ICEC, the reaction system includes the reactants' (ethane and CO₂) adsorption, activation, reaction, and products' (ethylene, CO, and H₂O) formation, and desorption. The apparent activation energies (E_a) for ethane conversion and CO₂ conversion are key to evaluating the rate matching of both reactions. Figure 2d shows similar E_a (results were calculated based on Fig. 2c and Supplementary Fig. 22) for ethane dehydrogenation (70.9 kJ/mol) and CO₂ hydroxylation (74.0 kJ/mol). This further demonstrates the feasibility and success of the Zn–O–Cr ABCs concept for desired ICEC catalyst development.

Figure 2a and Supplementary Fig. 19 reveal that there is a clear correlation between the proportion of Zn^{δ+}-O-Cr⁶⁺ sites and ICEC performance. Pure Cr/SSZ-13 catalyst displayed slightly higher ethylene selectivity (95.4%) and higher U_{CO₂} (96.0%) than Zn₃Cr₁/SSZ-13 sample, but has the lowest C₂H₆ conversion (5.1%), CO₂ conversion (4.9%), TOF of C₂H₄ formation (0.20 mol mol_{Zn+Cr}⁻¹ h⁻¹). Increasing Zn contents in Zn–O–Cr ABCs, with Zn/Cr ratios from 1/2 to 3/1, has little effect on ethylene selectivity and U_{CO₂}. Instead, increased Zn contents promote higher conversion of C₂H₆ and CO₂, and leads to increased TOF of ethylene formation. Further increasing the Zn content to Zn/Cr ratio of 4/1, triggers lower ethane (14.4%) and CO₂ (11.7%) conversions, resulting in a much lower U_{CO₂} (81.5%). Pure Zn/SSZ-13 exhibited further decreased C₂H₆ (12.1%) and CO₂ (10.2%) conversions, compared with Zn₄Cr₁/SSZ-13. Therefore, we hypothesize that the Zn^{δ+} in the binuclear site of Zn^{δ+}-O-Cr⁶⁺ is the primary active site for C₂H₆ dehydrogenation. Interestingly, the Zn^{δ+} proportion also displays a correlation with CO₂ conversion, which indicates that the Zn^{δ+} sites are also involved in CO₂ adsorption, activation, or reaction. In previous studies, binuclear Zn–O–Zn catalysts have been reported to have a high activity in ethane or propane dehydrogenation, but lack the capacity of efficient CO₂ activation, leading to insufficient CO₂ utilization^{35,54,55}. In our study, the Zn₃Cr₁/SSZ-13 ABC with the highest amount of Zn^{δ+}-O-Cr⁶⁺ sites displayed -1.5 and -4-fold higher ethane dehydrogenation and CO₂ conversion performance than pure Zn and Cr catalysts, respectively (Fig. 2b), which indicates the Cr⁶⁺ site of Zn^{δ+}-O-Cr⁶⁺ is also involved in the activation and reaction of C₂H₆ and CO₂. From the above analyses, we conclude that the unique performance of Zn–O–Cr ABCs for ICEC relies on the atomic synergies within the Zn^{δ+}-O-Cr⁶⁺ site.

To study the atomic synergies between Zn^{δ+}-O-Cr⁶⁺ site in ICEC, we compared the C₂H₆ dehydrogenation performance of Zn₃Cr₁/SSZ-13 with pure Zn/SSZ-13 and Cr/SSZ-13 samples in the presence and absence of CO₂. In Fig. 2e, we found the CO₂ co-feeding significantly improved C₂H₆ conversion (19.8% vs. 10.7%) and C₂H₄ selectivity (93.0% vs. 85.0%) for Zn₃Cr₁/SSZ-13, with a high U_{CO₂} up to 94.4%. By contrast, for Zn/SSZ-13, CO₂ addition fails to enhance its C₂H₆ conversion (12.1% vs. 13.3%) but results in an increase in C₂H₄ selectivity (94.6% vs. 86.0%). The higher C₂H₄ selectivity is due to competitive adsorption of CO₂ over C₂H₆, preventing the ethane cracking reaction,

which has been reported previously⁵⁶. Compared with Zn/SSZ-13, the improved C₂H₆ conversion of the Zn₃Cr₁/SSZ-13 catalyst is due to the generation of Zn^{δ+} in Zn^{δ+}-O-Cr⁶⁺. For the Cr/SSZ-13 sample, CO₂ introduction results in a higher C₂H₆ conversion (5.1% vs 4.0%) with a high U_{CO₂} of 96%, but it did not change the C₂H₄ selectivity (95.4% vs 95.1%). Cr-based catalysts are reported to catalyze CO₂ and ethane conversion through the redox (or MvK) mechanism²⁰. CO₂ introduction could favor lattice oxygen replenishment to regenerate highly reactive Cr⁶⁺ species and shift the reaction equilibrium of C₂H₆ dehydrogenation, thus leading to a higher activity. These results indicate that a reaction synergy between ethane and CO₂ conversions could only occur at the atomically synergistic Zn^{δ+}-O-Cr⁶⁺ site.

To further validate the superiority of Zn–O–Cr ABCs, we compared the performance of Zn₃Cr₁/SSZ-13 prepared by the dry-deposition method with the sample synthesized by the traditional coprecipitation (CP) method. Supplementary Fig. 23 shows that the dry-deposition synthesized Zn₃Cr₁/SSZ-13 catalyst exhibited >4-fold higher ethane conversion (19.8% vs 4.5%) and higher U_{CO₂} (94.4% vs 83.2%). The CP-synthesized Zn₃Cr₁/SSZ-13 sample was found to contain large Zn/Cr oxide particles and separate ZnCr₂O₄ and ZnO phases, resulting in loss of the atomic synergies of the Zn^{δ+}-O-Cr⁶⁺ site, which we correlate with its poor performance. We also studied the stability and regeneration ability of the Zn₃Cr₁/SSZ-13 ABC catalyst. Supplementary Fig. 24 shows that the ethylene selectivity and U_{CO₂} remained nearly 100% during a total of 150 h in 3 cycles. And the decayed conversion of ethane and CO₂ can be totally regenerated by oxidative treatment in air at 500 °C. This excellent durability and regeneration ability demonstrates the structural stability of Zn^{δ+}-O-Cr⁶⁺ site.

Electronic structure of binuclear Zn^{δ+}-O-Cr⁶⁺ sites during the reaction

In situ ambient pressure X-ray photoelectron spectroscopy (APXPS) was employed to examine the electronic structure of binuclear Zn^{δ+}-O-Cr⁶⁺ sites and study the atomic synergies between Zn^{δ+} and Cr⁶⁺ sites in ICEC. Figure 3a–c shows ambient pressure spectra indicating C 1s binding energies, Zn LMM Auger kinetic energies, and Cr 2p_{3/2} binding energies.

Step 1: Zn₃Cr₁/SSZ-13 was first tested under 550 °C in an ultra-high vacuum (UHV). The temperature of 550 °C was used to match the reaction temperature in Fig. 2. In Auger spectra of Zn LMM (Fig. 3b), both Zn²⁺ (dark blue) and Zn^{δ+} (green) species were detected with a percentage distribution of 72.4% and 27.6%, respectively. In Fig. 3c, Cr³⁺ (dark red) and Cr⁶⁺ (light blue) were detected with a proportion of 50.6% and 49.4%, respectively.

Step 2: Then the Zn₃Cr₁/SSZ-13 was subjected to simulated reaction conditions of ICEC by co-feeding 50 mTorr C₂H₆ and 50 mTorr CO₂ under 550 °C. The signals of gaseous C₂H₆ and CO₂ were detected in Fig. 3a. Notably, adsorbed CO species (CO_{ads}) at 285.5 eV were observed^{57,58}, which indicates the ICEC reaction occurred. Under the reaction conditions, the proportion of Zn^{δ+} decreased (from 27.6% to 22.8%) and Cr⁶⁺ ratio increased (from 49.4% to 54.4%). DFT calculations (Fig. 3d) indicate that the oxidation from Zn^{δ+} to Zn²⁺ is due to the formation of Zn–H^δ hydride during the ethane dehydrogenation, with more negative charge accumulated on H^δ. The oxidation of Cr³⁺ to Cr⁶⁺ may result from lattice oxygen replenishment via CO₂ dissociation²⁰. These results indicate both Zn^{δ+} and Cr⁶⁺ were involved in the ICEC reaction.

Steps 3 and 4 were designed to understand the role of individual Zn^{δ+} or Cr⁶⁺ in ICEC. When feeding 100 mTorr C₂H₆ (without CO₂) in step 3 (Fig. 3a, b), the signals of CO₂ and CO_{ads} species disappeared, which indicates that only ethane dehydrogenation could occur. The proportions of Zn²⁺ and Zn^{δ+} remain similar to the case of co-feeding C₂H₆ and CO₂ in step 2, indicating the formation of Zn–H^δ hydride during the ethane dehydrogenation. Notice that the proportions of Zn^{δ+} and Zn²⁺ are comparable between step 1 (UHV) and step 4

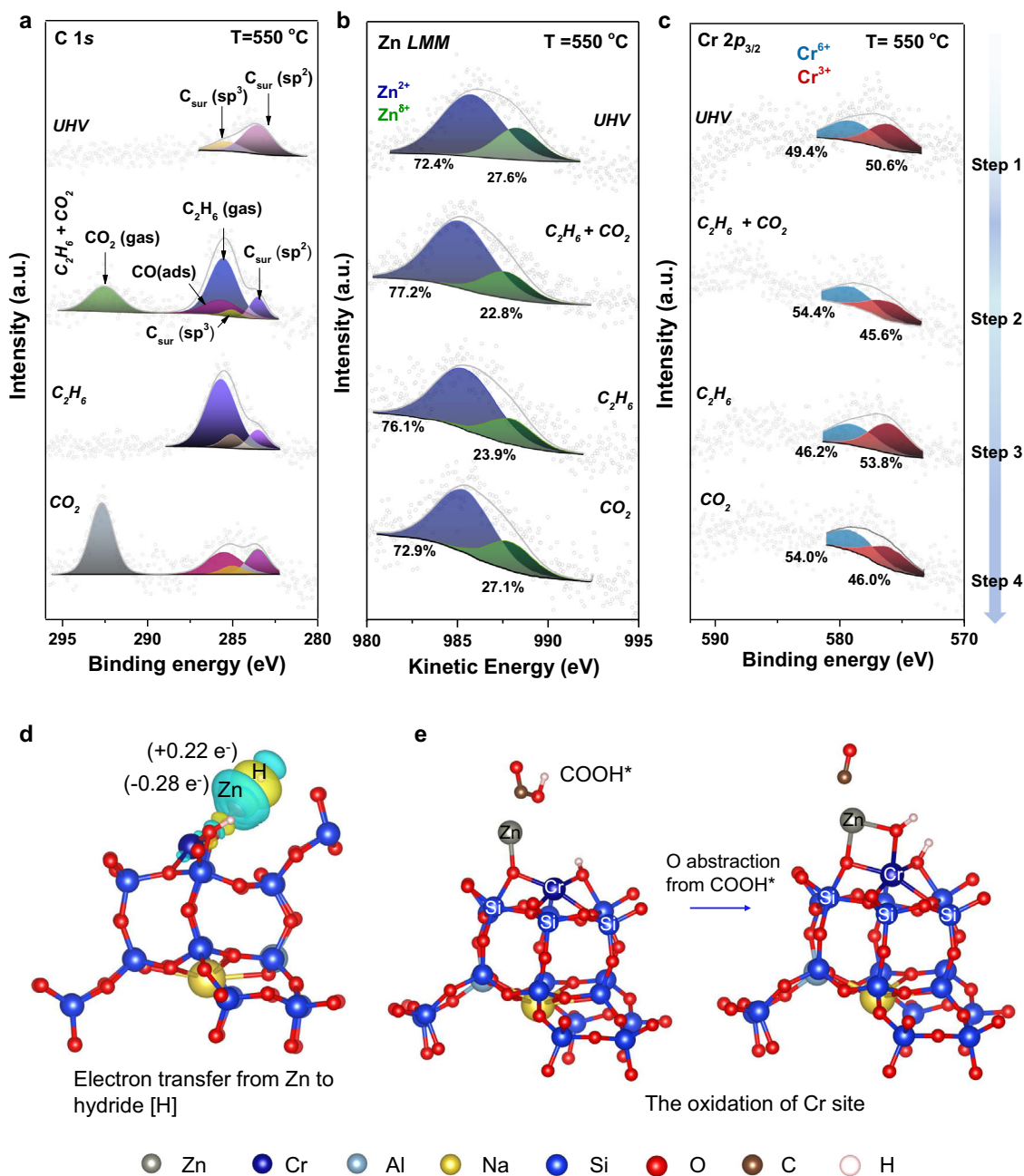


Fig. 3 | Electronic structure changes of binuclear $\text{Zn}^{\delta+}$ -O- Cr^{6+} sites. In situ ambient pressure X-ray photoelectron spectroscopy (APXPS): **a** C 1s spectra, **b** Auger spectra of Zn LMM, and **c** Cr $2p_{3/2}$ spectra as a function of reaction conditions for $\text{Zn}_3\text{Cr}_1/\text{SSZ-13}$. $T = 550^\circ\text{C}$: ultra-high vacuum (UHV), C_2H_6 (50 mTorr) + CO_2 (50 mTorr), C_2H_6 (100 mTorr), and CO_2 (100 mTorr) in sequence. **d** Electron transfer from Zn to

H after the 2nd C-H bond scission in ethane (H: white; Zn: gray), where electron accumulation and depletion are represented by yellow ($\Delta\rho = +1 \times 10^{-3} \text{ e bohr}^{-3}$) and cyan ($\Delta\rho = -1 \times 10^{-3} \text{ e bohr}^{-3}$) respectively. **e** The oxidation of Cr in Zn-O-Cr when decomposing COOH^* intermediate.

(feeding 100 mTorr CO_2 without ethane), ruling out the likelihood of oxidation of $\text{Zn}^{\delta+}$ to Zn^{2+} by CO_2 or its derived intermediates.

In the case of Cr $2p_{3/2}$ XPS spectra (Fig. 3c), the oxidation of Cr^{3+} to Cr^{6+} only occurs when CO_2 was fed (steps 2 and 4). Previous studies have demonstrated the oxidation of Cr^{3+} to Cr^{6+} in Cr-based catalysts suffers from sluggish O abstraction from CO_2 ^{20,59}. In our cases, the facile reoxidation of Cr^{3+} to Cr^{6+} may be due to the possibility that nearby $\text{Zn}^{\delta+}$ facilitate the CO_2 activation to enable easier O abstraction. The CO_{ads} species at 285.5 eV were detected in the presence/co-presence of CO_2 in the C 1s spectra (Fig. 3a, steps 2 and 4), which further demonstrates facile CO_2 dissociation over the $\text{Zn}^{\delta+}$ -O- Cr^{6+} site. Our DFT calculation (Fig. 3e) indicates that the intermediate of CO_2

activation is carboxyl (COOH^*). The decomposition of COOH^* requires the participation of the Cr site through the formation of a new Cr-O bond ($d(\text{Cr}-\text{O}) = 2.08 \text{ \AA}$), which will maintain its high oxidation state. In summary, the APXPS results show that binuclear $\text{Zn}^{\delta+}$ -O- Cr^{6+} sites serve as atomically synergistic sites for ICEC.

Atomically synergistic mechanism

We developed atomically synergistic mechanisms for ICEC on binuclear Zn-O-Cr sites (Fig. 4 and Supplementary Fig. 30-35, Supplementary Tables 8-10). Figure 4a shows that the catalytic cycle is initiated by C_2H_6 adsorption on Zn ([1] [2]), then heterolytic cleavage of the first C-H bond (0.93 eV) by breaking a Zn-O-Cr bond to form $\text{Zn}-\text{CH}_2-\text{CH}_3$

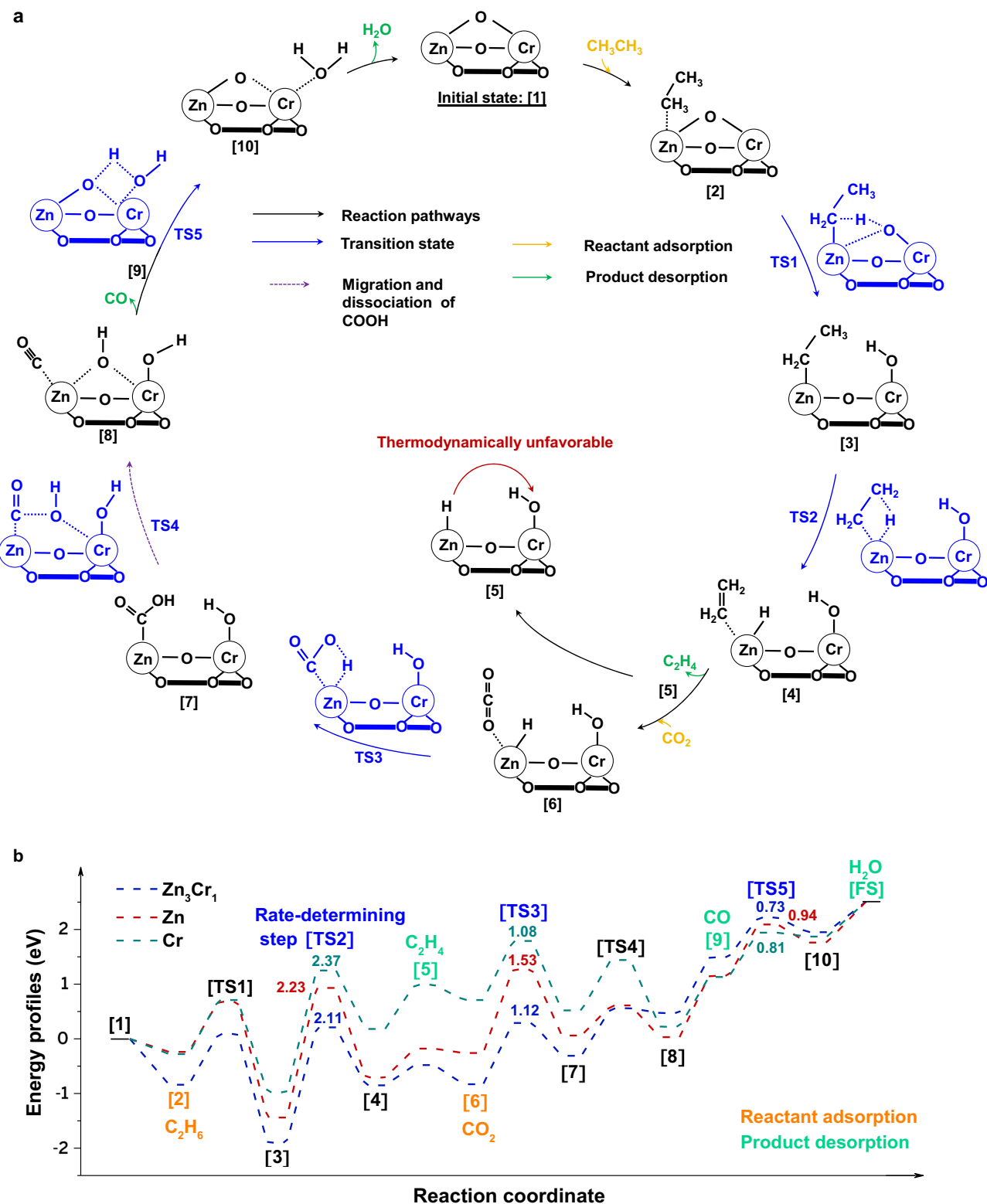


Fig. 4 | Atomically synergistic mechanism of ICEC over binuclear Zn-O-Cr sites. a Catalytic cycles of ICEC over binuclear Zn-O-Cr sites of Zn₃Cr₁/SSZ-13. **b** The calculated energy profiles of ICEC on Zn₃Cr₁/SSZ-13, Zn/SSZ-13, and Cr/SSZ-13.

and Cr-OH ([2] [3]), followed by a homolytic scission of the β -C-H bond (2.11 eV) ([3] [4]), and finally, C₂H₄ desorption and Zn-H^{δ-} hydride formation ([4] [5]). C₂H₆ activation at the Cr of Zn-O-Cr sites has higher energy barriers for the first C-H cleavage (1.78 eV vs 0.93 eV) and β -C-H bond dissociation (>3.0 eV vs 2.11 eV), leading to a kinetically unfavorable pathway (Supplementary Figs. 31 and 32). In the second stage

(Fig. 4a), CO₂ prefers to adsorb at Zn-H^{δ-} site (-0.35 eV) than the Cr site (-0.05 eV) through acid-base interaction (Supplementary Fig. 33) ([5] [6])^{60,61}; CO₂ adsorption energy (-0.35 eV) at Zn-H^{δ-} site is lower than ethane adsorption (-0.17 eV), which will help prevent the C₂H₆ cracking reaction (Supplementary Table 5). Then Zn-H^{δ-} enables CO₂ hydrogenation ([6][7]) to carboxyl (COOH*), followed by CO-OH

cleavage and migration of -OH to be shared with Cr ([7][8]). Finally, after CO desorption from the Zn site and the formation and desorption of H₂O from the Cr site to replenish lattice oxygen ([8][10]), the ICEC catalytic cycle is closed.

The simulated catalytic cycles of Zn/SSZ-13 and Cr/SSZ-13 are shown in Supplementary Figs. 34 and 35, and the calculated energy profiles of ICEC over Zn₃Cr₁/SSZ-13, Zn/SSZ-13, and Cr/SSZ-13 are presented in Fig. 4b. The rate-determining step of ICEC is the homolytic cleavage of the β-C-H bond in ethane activation [TS2] (Fig. 4b, Supplementary Table 9). Zn₃Cr₁/SSZ-13 exhibited a lower activation barrier (2.11 eV) than Zn/SSZ-13 (2.37 eV) and Cr/SSZ-13 (2.23 eV). Moreover, Zn₃Cr₁/SSZ-13 also displayed a much lower energy barrier (1.12 eV, 0.73 eV) for CO₂ activation [TS3] and H₂O formation [TSS] than Zn/SSZ-13 (1.53 eV, 0.94 eV). This explained the much higher CO₂ conversion and utilization of Zn₃Cr₁/SSZ-13 catalyst than Zn/SSZ-13 catalyst (Fig. 2b). We also found that Zn₃Cr₁/SSZ-13 exhibited the most favorable energetics of reactants adsorption and products desorption which also helps accelerate catalytic reactions (Supplementary Table 10). Therefore, the kinetically and thermodynamically favorable elementary steps in the ICEC catalytic cycle result in the highest catalytic performance of Zn₃Cr₁/SSZ-13. Its superior performance in ICEC is due to the atomic synergies between the acidic Zn site and the redox Cr site of ABC.

Discussion

In this study, we demonstrated the advantages of an atomically-synergistic binuclear-site catalyst (ABC) synthesized by colocalizing Zn and Cr sites on a zeolite SSZ-13 support (ZnCr/SSZ-13) for the stoichiometric co-conversion of ethane and CO₂ (ICEC) reaction. This ZnCr ABC catalyst exhibited exceptional catalytic performance, with 100% ethylene selectivity and 99.0% U_{CO₂} under optimized conditions. The combined results of XAS, AP-XPS, and DFT studies show that the electronic properties and catalytic activity of ZnCr/SSZ-13 can be precisely assigned to unique atomic synergies between neighboring Zn and Cr atoms resulting from colocalization. The redox Cr site facilitates the formation of Zn^{δ+}, which is the active site for easier adsorption and activation of both ethane and CO₂. Furthermore, the Cr site accelerates CO₂ dissociation, due to its redox properties, and facilitates the formation and desorption of H₂O. This combination thus results in rate matching between ethane dehydrogenation and CO₂ hydrogenation. Our study highlights the importance of atomic synergy, providing guidance for developing novel catalysts with potential economic and ecological benefits in CO₂ conversion and olefin production.

Methods

Materials synthesis. Zn_xCr_y/SSZ-13 ($x=1, y=0; x/y=1/2, 1, 2, 3, \text{ and } 4; x=0, y=1$) catalysts were prepared by the dry-deposition method⁶². The total amount of Zn and Cr in all catalysts was set at 0.8 mmol per 1 g of support materials. In a typical synthesis, the SSZ-13 zeolite support was pretreated in a vacuum at 120 °C for 3 h to remove moisture. The stoichiometric amount of Zinc (II) acetate and/or chromium (III) acetate hydroxide (Zn + Cr = 0.8 mmol) was thoroughly mixed with 1 g of SSZ-13 zeolites using an analog vortex mixer. The resulting solid mixtures were sufficiently ground in glove box for 20 min. Subsequently, the samples are heated in flowing N₂ (100 mL/min) at 550 °C for 3 h at a ramping rate of 2 °C/min and subsequently in flowing air (100 mL/min) for another 3 h. Both N₂ and air were purified by moisture trap (Restek). Afterward, the resulting materials were pretreated through Na⁺-neutralization. Typically, the sample was firstly dispersed in deionized water and then dropwise addition of sodium bicarbonate solution (0.01 M, pH = 8) was performed until the solution reached a pH of 7. The slurry was then collected and dried at 110 °C overnight. The samples were finally calcined in static air at 500 °C for 2 h with a ramping rate of 2 °C/min. The final products were stored in

an N₂ box. The control samples of Zn_xCr/SSZ-13 ($x=1/2, 1, \text{ and } 3$) were synthesized using the traditional co-precipitation (CP) method according to the reported recipe⁴¹, followed by Na⁺ neutralization.

Materials characterization. Nitrogen physisorption was performed on the Quantachrome Autosorb iQ2 instrument at 77 K to obtain textural information. The surface area (S_{BET}) was determined from the N₂ isotherms using the Brunauer-Emmett-Teller (BET) method. X-ray fluorescence (XRF) measurements were performed with a EDAX Orbis Micro-XRF Spectrometer. The attenuated total reflection Fourier transform infrared (ATR-FTIR) measurements were conducted by a Thermo Nicolet iS50 FTIR spectrometer with a diamond crystal ATR module. Powder X-ray diffraction (XRD) analysis was performed on a Rigaku MiniFlex 6 G X-Ray Diffractometer (Cu K_α radiation with wavelength of 1.5406 Å). The transmission electron microscopy (TEM) experiments were performed on a FEI ThemIS aberration-corrected TEM at the National Center for Electron Microscopy (NCEM) of the Molecular Foundry (MF), Lawrence Berkeley National Laboratory (LBNL). The microscope was operated at 300 keV with a Super-X energy dispersive X-ray spectroscopy (EDS) detector, allowing for rapid chemical identification. X-ray photoelectron spectroscopy (XPS) measurement was conducted at a K-Alpha Plus XPS spectrometer (Thermo Scientific), which consists of a monochromatic Al X-ray source (Al K_α = 1,486.68 eV) with variable spot size ranging from 30 microns to 400 microns. Powder samples were placed on a double-sided silver tape and the spectra were acquired using the flood-gun source to account for surface charging. All the spectra were analyzed using the CasaXPS software package.

Zn L₃-edge soft X-ray absorption spectroscopy (sXAS) measurement was performed at Beamline 7.3.1 of the Advanced Light Source (ALS) at Lawrence Berkeley National Laboratory (LBNL). sXAS measurement was collected at room temperature through total electron yield (TEY) mode with a probe depth of no more than 10 nm. All the TEY spectra were normalized to the beam flux.

The measurements of Zn K-edge and Cr K-edge XAS spectra including X-ray absorption near edge structure (XANES) and extended X-ray absorption fine structure (EXAFS) were performed at TPS 44 A beamline in National Synchrotron Radiation Research Center (NSRRC) in Taiwan. The data were collected in fluorescence mode by using 7-element silicon drift detector and the Zn and Cr metal foil were used as references for the energy calibration. The data were processed according to standard procedures using Demeter program package.

Ambient-pressure XPS (AP-XPS) analysis was conducted at Sandia National Laboratories (Livermore, CA) using a differentially-pumped Al K_α source (Specs model XR50) with a photon energy of 1486.6 keV. Emitted photo- (and Auger) electrons were detected using a near-ambient pressure hemispherical analyzer (Specs model Phoibos 150) mounted in a custom designed system capable of measuring XPS under sample gas pressures up to 10 Torr. We used baked steel gas lines and leak valves to introduce C₂H₆ (99.995% pure) and CO₂ (99.999% pure) from Matheson Tri-Gas Inc. XPS/Auger peak locations, widths, and areas were obtained using a Shirley background subtraction and by fitting the data to mixed Gaussian-Lorentzian line shapes using CasaXPS software.

Performance Tests. The catalytic performance of stoichiometric co-conversion of ethane and CO₂ (ICEC) was conducted on a continuous fix-bed reactor in the temperature range of 400–550 °C and under ambient pressure, which is held inside an electric furnace with temperature controlled by a K-type thermocouple. In a typical catalytic measurement, a total of 200 mg catalyst diluted by 800 mg sand was loaded into the middle of the reactor plugged by quartz wool on two sides. Before the catalytic test, the catalyst bed was pretreated under a flow of Argon (25 sccm) at 550 °C for 1 h with a ramping rate of 10 °C from room temperature. Afterward, the reactant mixtures consisting of 5% CO₂, and 5% C₂H₆ balanced with Argon were introduced with a total flow rate of 25 sccm. Argon is used

as an internal standard. The reaction products were analyzed by online GC (Agilent 5890, ShinCarbon ST Packed Columns) equipped with thermal conductivity detector (TCD) and flame ionization detector (FID). To better reveal the reaction kinetics, apparent activation barriers were determined in the temperature range of 400–475 °C (The conversions of CO₂ and C₂H₆ are less than 10%). The carbon and oxygen balances were within 100 ± 2% for all tests. The conversions of CO₂ and C₂H₆, C₂H₄ selectivity, utilization of converted CO₂ (U_{CO₂}), C₂H₄ yield, the turnover frequency (TOF) of C₂H₄ formation, and the space time yield (STY) of C₂H₄ formation were calculated as follows (where n denotes molar flow of substance (mol/min), n_{Zn+Cr} means the total molar loading of Zn and/or Cr, M_{C₂H₄} is the molecular weight of C₂H₄ (28 g/mol) and m_{cat} stands for catalyst mass (kg)):

$$\text{CO}_2 \text{ conversion (\%)} = \frac{n_{\text{CO}_2 \text{ input}} - n_{\text{CO}_2 \text{ output}}}{n_{\text{CO}_2 \text{ input}}} \times 100\% \quad (1)$$

$$\text{C}_2\text{H}_6 \text{ conversion (\%)} = \frac{n_{\text{C}_2\text{H}_6 \text{ input}} - n_{\text{C}_2\text{H}_6 \text{ output}}}{n_{\text{C}_2\text{H}_6 \text{ input}}} \times 100\% \quad (2)$$

$$\text{C}_2\text{H}_4 \text{ selectivity (\%)} = \frac{n_{\text{C}_2\text{H}_4 \text{ output}}}{n_{\text{C}_2\text{H}_6 \text{ input}} - n_{\text{C}_2\text{H}_6 \text{ output}}} \times 100\% \quad (3)$$

$$U_{\text{CO}_2} \text{ (\%)} = \frac{\text{CO}_2 \text{ conversion}}{\text{C}_2\text{H}_6 \text{ conversion}} \times 100\% \quad (4)$$

$$\text{C}_2\text{H}_4 \text{ yield (\%)} = \text{C}_2\text{H}_6 \text{ conversion} \times \text{C}_2\text{H}_4 \text{ selectivity} \quad (5)$$

$$\text{TOF} = \frac{n_{\text{C}_2\text{H}_4 \text{ output}} \times 60}{n_{\text{Zn+Cr}}} \quad (6)$$

$$\text{STY} = \frac{n_{\text{C}_2\text{H}_4 \text{ output}} \times M_{\text{C}_2\text{H}_4} \times 60}{1000 \times m_{\text{cat}}} \quad (7)$$

It is noted that calculations of U_{CO₂} were also calibrated and examined by the equation:

$$U_{\text{CO}_2} \text{ (\%)} = \frac{n_{\text{CO}_2 \text{ output}}}{n_{\text{C}_2\text{H}_6 \text{ input}} - n_{\text{C}_2\text{H}_6 \text{ output}}} \times 100\% \quad (8)$$

Computational Methods. All DFT calculations were performed using Vienna ab initio simulation package (VASP)^{63,64}. The projector-augmented wave (PAW) method was used to represent the core-valence electron interaction^{65,66}. The generalized gradient approximation (GGA) with the Perdew–Burke–Ernzerhof (PBE) exchange-correlation functional was used with D3 dispersion correction^{67,68}. The cutoff energy for the planewave basis was 500 eV. To accurately treat the highly localized transition metal 3d orbitals, the spin-polarized DFT + U approach^{69,70} was employed: U_{eff} = 4.7 and 3.0 eV were applied to the Zn 3d and Cr 3d state, respectively^{71,72}. Electronic energies were converged to within 10⁻⁴ eV and the atomic positions were relaxed until the force on each atom was less than 0.05 eV/Å. The climbing-image nudged elastic band (CI-NEB) method⁷³ was used to search for the transition states. A hexagonal unit cell of the SSZ-13 molecular sieve⁷⁴ was used as the support: a = b = 13.72 Å, c = 14.95 Å; composition: Na₁Al₁Si₃O₇₂. Only the Γ-point was used to sample the Brillouin zone. The unit cell contains two hexagonal prisms; two units of Zn₂O₂ and Cr₂O₃ were placed on the two prisms, to create the models of Zn/SSZ-13 and Cr/SSZ-13, respectively; one Zn₂O₂ unit was placed on one of the prisms and one ZnCrO₂ unit on the other, to create the model of Zn₃Cr₁/SSZ-13 (see Supplementary Fig. 30).

Data availability

The data that supports the findings of this study are available from the corresponding authors upon request.

References

- Wang, H. et al. Strong metal–support interactions on gold nanoparticle catalysts achieved through Le Chatelier’s principle. *Nat. Catal.* **4**, 418–424 (2021).
- Parastaev, A. et al. Boosting CO₂ hydrogenation via size-dependent metal–support interactions in cobalt/ceria-based catalysts. *Nat. Catal.* **3**, 526–533 (2020).
- Van Deelen, T. W., Hernández Mejía, C. & De Jong, K. P. Control of metal–support interactions in heterogeneous catalysts to enhance activity and selectivity. *Nat. Catal.* **2**, 955–970 (2019).
- Chen, A. et al. Structure of the catalytically active copper–ceria interfacial perimeter. *Nat. Catal.* **2**, 334–341 (2019).
- Lunkenbein, T., Schumann, J., Behrens, M., Schlögl, R. & Willinger, M. G. Formation of a ZnO overlayer in industrial Cu/ZnO/Al₂O₃ catalysts induced by strong metal–support interactions. *Angew.-Chem. Int. Ed.* **54**, 4544–4548 (2015).
- Pu, T., Zhang, W. & Zhu, M. Engineering heterogeneous catalysis with strong metal–support interactions: characterization, theory and manipulation. *Angew. Chem. Int. Ed.* **62**, e202212278 (2023).
- Li, Y., Zhang, Y., Qian, K. & Huang, W. Metal–support interactions in metal/oxide catalysts and oxide–metal interactions in oxide/metal inverse catalysts. *ACS Catal.* **12**, 1268–1287 (2022).
- Zhang, L., Zhou, M., Wang, A. & Zhang, T. Selective hydrogenation over supported metal catalysts: from nanoparticles to single atoms. *Chem. Rev.* **120**, 683–733 (2020).
- Shi, J. On the synergetic catalytic effect in heterogeneous nanocomposite catalysts. *Chem. Rev.* **113**, 2139–2181 (2013).
- Ro, I. et al. Bifunctional hydroformylation on heterogeneous Rh–WO_x pair site catalysts. *Nature* **609**, 287–292 (2022).
- Gao, R. et al. Pt/Fe₂O₃ with Pt–Fe pair sites as a catalyst for oxygen reduction with ultralow Pt loading. *Nat. Energy* **6**, 614–623 (2021).
- Liu, C. et al. Catalytic activity enhancement on alcohol dehydrogenation via directing reaction pathways from single- to double-atom catalysis. *J. Am. Chem. Soc.* **144**, 4913–4924 (2022).
- Yang, J. et al. Modulating the strong metal–support interaction of single-atom catalysts via vicinal structure decoration. *Nat. Commun.* **13**, 4244 (2022).
- Li, W. H., Yang, J. & Wang, D. Long-range interactions in diatomic catalysts boosting electrocatalysis. *Angew. Chem. Int. Ed.* **61**, e202213318 (2022).
- Pan, Y., Zhang, C., Liu, Z., Chen, C. & Li, Y. Structural regulation with atomic-level precision: from single-atomic site to diatomic and atomic interface. *Catal. Matter* **2**, 78–110 (2020).
- Zeng, Z. et al. Orbital coupling of hetero-diatom nickel–iron site for bifunctional electrocatalysis of CO₂ reduction and oxygen evolution. *Nat. Commun.* **12**, 4088 (2021).
- Zheng, X. et al. Ru–Co pair sites catalyst boosts the energetics for the oxygen evolution reaction. *Angew. Chem. Int. Ed.* **61**, e202205946 (2022).
- Guan, E. et al. Supported metal pair-site catalysts. *ACS Catal.* **10**, 9065–9085 (2020).
- Mitchell, S. & Pérez-Ramírez, J. Atomically precise control in the design of low-nuclearity supported metal catalysts. *Nat. Rev. Mater.* **6**, 969–985 (2021).
- Gomez, E., Yan, B., Kattel, S. & Chen, J. G. Carbon dioxide reduction in tandem with light-alkane dehydrogenation. *Nat. Rev. Chem.* **3**, 638–649 (2019).
- Biswas, A. N., Xie, Z. & Chen, J. G. Can CO₂-assisted alkane dehydrogenation lead to negative CO₂ emissions? *Joule* **6**, 269–273 (2022).

22. Myint, M. N. Z., Yan, B., Wan, J., Zhao, S. & Chen, J. G. Reforming and oxidative dehydrogenation of ethane with CO₂ as a soft oxidant over bimetallic catalysts. *J. Catal.* **343**, 168–177 (2016).
23. Xie, Z. et al. Reactions of CO₂ and ethane enable CO bond insertion for production of C3 oxygenates. *Nat. Commun.* **11**, 1887 (2020).
24. Chatani, Y., Takizawa, T., Murahashi, S., Sakata, Y. & Nishimura, Y. Crystal structure of polyketone (1: 1 Ethylene/Carbon Monoxide Copolymer). *J. Polym. Sci.* **55**, 811–819 (1961).
25. Brubaker, M. M., Coffman, D. D. & Hoehn, H. H. Synthesis and characterization of ethylene/carbon monoxide copolymers, a new class of polyketones. *J. Am. Chem. Soc.* **74**, 1509–1515 (1952).
26. Chen, S. et al. Cationic P,O-coordinated Nickel(II) catalysts for carbonylative polymerization of ethylene: unexpected productivity via subtle electronic variation. *Angew. Chem. Int. Ed.* **61**, e202204126 (2022).
27. Ortmann, P., Wimmer, F. P. & Mecking, S. Long-spaced polyketones from ADMET copolymerizations as ideal models for ethylene/CO copolymers. *ACS Macro Lett.* **4**, 704–707 (2015).
28. Xie, Z., Wang, X., Chen, X., Liu, P. & Chen, J. G. General descriptors for CO₂-assisted selective C-H/C-C bond scission in ethane. *J. Am. Chem. Soc.* **144**, 4186–4195 (2022).
29. Kattel, S., Chen, J. G. & Liu, P. Mechanistic study of dry reforming of ethane by CO₂ on a bimetallic PtNi(111) model surface. *Catal. Sci. Technol.* **8**, 3748–3758 (2018).
30. Guo, H., Xie, Z., Wang, X., Chen, J. G. & Liu, P. Descriptor-based identification of bimetallic-derived catalysts for selective activation of ethane with CO₂. *EES Catal.* **1**, 17–25 (2023).
31. Li, G., Liu, C., Cui, X., Yang, Y. & Shi, F. Oxidative dehydrogenation of light alkanes with carbon dioxide. *Green Chem.* **23**, 689–707 (2021).
32. Najari, S. et al. Oxidative dehydrogenation of ethane: catalytic and mechanistic aspects and future trends. *Chem. Soc. Rev.* **50**, 4564–4605 (2021).
33. Zhao, D. et al. Controlling reaction-induced loss of active sites in ZnO_x/Silicalite-1 for durable nonoxidative propane dehydrogenation. *ACS Catal.* **12**, 4608–4617 (2022).
34. Schweitzer, N. M. et al. Propylene hydrogenation and propane dehydrogenation by a single-site Zn²⁺ on silica catalyst. *ACS Catal.* **4**, 1091–1098 (2014).
35. Zhao, D. et al. In situ formation of ZnO_x species for efficient propane dehydrogenation. *Nature* **599**, 234–238 (2021).
36. Liu, X. et al. In situ spectroscopic characterization and theoretical calculations identify partially reduced ZnO_{1-x}/Cu interfaces for methanol synthesis from CO₂. *Angew. Chem. Int. Ed.* **134**, e202202330 (2022).
37. Consonni, M., Jokic, D., Murzin, D. Y. & Touroude, R. High performances of Pt/ZnO catalysts in selective hydrogenation of crotonaldehyde. *J. Catal.* **188**, 165–175 (1999).
38. Hsu, J. Y. et al. Probing local structural changes by sharp luminescent infrared nanophosphor for application in light-emitting diodes. *Chem. Mater.* **34**, 11093–11100 (2022).
39. Liu, B. M. et al. A High-efficiency blue-LED-excitable NIR-II-emitting MgO:Cr³⁺,Ni²⁺ phosphor for future broadband light source toward multifunctional NIR spectroscopy applications. *Chem. Eng. J.* **452**, 139313 (2023).
40. Jiao, F. et al. Selective conversion of syngas to light olefins. *Science* **351**, 1065–1068 (2016).
41. Yang, F. et al. One-step alkylation of benzene with Syngas over non-noble catalysts mixed with modified HZSM-5. *Ind. Eng. Chem. Res.* **58**, 13879–13888 (2019).
42. Song, H. et al. Spinel-structured ZnCr₂O₄ with excess Zn is the active ZnO/Cr₂O₃ catalyst for high-temperature methanol synthesis. *ACS Catal.* **7**, 7610–7622 (2017).
43. Li, S. et al. Low-valence Zn^{δ+} (0<δ<2) single-atom material as highly efficient electrocatalyst for CO₂ reduction. *Angew. Chem. Int. Ed.* **60**, 22826–22832 (2021).
44. Li, X. et al. Improved catalytic performance of ethane dehydrogenation in the presence of CO₂ over Zr-promoted Cr/SiO₂. *ACS Omega* **4**, 22562–22573 (2019).
45. Dadlani, A. et al. Revealing the bonding environment of Zn in ALD Zn(O,S) buffer layers through X-ray absorption spectroscopy. *ACS Appl. Mater. Interfaces* **9**, 39105–39109 (2017).
46. Qiao, L. et al. The impact of crystal symmetry on the electronic structure and functional properties of complex lanthanum chromium oxides. *J. Mater. Chem. C* **1**, 4527–4535 (2013).
47. Ramirez, A. et al. Multifunctional catalyst combination for the direct conversion of CO₂ to propane. *JACS Au* **1**, 1719–1732 (2021).
48. Pinilla-Herrero, I. et al. High Zn/Al ratios enhance dehydrogenation vs hydrogen transfer reactions of Zn-ZSM-5 catalytic systems in methanol conversion to aromatics. *J. Catal.* **362**, 146–163 (2018).
49. Thirumala Bai, P. et al. Oxidative dehydrogenation of ethane with carbon dioxide over Cr₂O₃/SBA-15 catalysts: the influence of sulfate modification of the support. *Appl. Petrochem. Res.* **7**, 107–118 (2017).
50. Talati, A., Haghghi, M. & Rahmani, F. Oxidative dehydrogenation of ethane to ethylene by carbon dioxide over Cr/TiO₂-ZrO₂ nanocatalyst: effect of active phase and support composition on catalytic properties and performance. *Adv. Powder Technol.* **27**, 1195–1206 (2016).
51. Shen, Z. et al. Dehydrogenation of ethane to ethylene over a highly efficient Ga₂O₃/HZSM-5 catalyst in the presence of CO₂. *Appl. Catal. A Gene.* **356**, 148–153 (2009).
52. Bugrova, T. A. et al. Oxidative dehydrogenation of ethane with CO₂ over CrO_x catalysts supported on Al₂O₃, ZrO₂, CeO₂ and Ce_xZr_{1-x}O₂. *Catal. Today* **333**, 71–80 (2019).
53. Koirala, R., Buechel, R., Krumeich, F., Pratsinis, S. E. & Baiker, A. Oxidative dehydrogenation of ethane with CO₂ over flame-made Ga-loaded TiO₂. *ACS Catal.* **5**, 690–702 (2015).
54. Liu, J. et al. Influence of the zeolite surface properties and potassium modification on the Zn-catalyzed CO₂-assisted oxidative dehydrogenation of ethane. *Appl. Catal. B Environ.* **304**, 120947 (2022).
55. Liu, J. et al. Highly-dispersed zinc species on zeolites for the continuous and selective dehydrogenation of ethane with CO₂ as a soft oxidant. *ACS Catal.* **11**, 2819–2830 (2021).
56. Tu, C. et al. CO₂-assisted ethane aromatization over zinc and phosphorous modified ZSM-5 catalysts. *Appl. Catal. B Environ.* **304**, 120956 (2022).
57. Miller, A. V., Kaichev, V. V., Prosvirin, I. P. & Bukhtiyarov, V. I. Mechanistic study of methanol decomposition and oxidation on Pt(111). *J. Phys. Chem. C* **117**, 8189–8197 (2013).
58. Wu, C. H., Eren, B., Bluhm, H. & Salmeron, M. B. Ambient-pressure X-ray photoelectron spectroscopy study of cobalt foil model catalyst under CO, H₂, and their mixtures. *ACS Catal.* **7**, 1150–1157 (2017).
59. Mimura, N., Takahara, I., Inaba, M., Okamoto, M. & Murata, K. High-performance Cr/H-ZSM-5 catalysts for oxidative dehydrogenation of ethane to ethylene with CO₂ as an oxidant. *Catal. Commun.* **3**, 257–262 (2002).
60. Álvarez, A. et al. CO₂ activation over catalytic surfaces. *Chem-PhysChem* **18**, 3135–3141 (2017).
61. Zimmerman, P. M., Zhang, Z. & Musgrave, C. B. Simultaneous two-hydrogen transfer as a mechanism for efficient CO₂ reduction. *Inorg. Chem.* **49**, 8724–8728 (2010).
62. Peeters, E. et al. Highly dispersed Sn-beta zeolites as active catalysts for Baeyer-Villiger oxidation: the role of mobile, in situ Sn(II)O species in solid-state stannation. *ACS Catal.* **11**, 5984–5998 (2021).
63. Kresse, G. & Furthmüller, J. Efficiency of ab-initio total energy calculations for metals and semiconductors using a plane-wave basis set. *Comput. Mater. Sci.* **6**, 15–50 (1996).
64. Kresse, G. & Furthmüller, J. Efficient iterative schemes for ab initio total-energy calculations using a plane-wave basis set. *Phys. Rev. B* **54**, 11169–11186 (1996).

65. Blöchl, P. E., Jepsen, O. & Andersen, O. K. Improved tetrahedron method for Brillouin-zone integrations. *Phys. Rev. B* **49**, 16223–16233 (1994).
66. Kresse, G. & Joubert, D. From ultrasoft pseudopotentials to the projector augmented-wave method. *Phys. Rev. B* **59**, 1758–1775 (1999).
67. Grimme, S., Antony, J., Ehrlich, S. & Krieg, H. A consistent and accurate ab initio parametrization of density functional dispersion correction (DFT-D) for the 94 elements H–Pu. *J. Chem. Phys.* **132**, 154104 (2010).
68. Perdew, J. P., Burke, K. & Ernzerhof, M. Generalized gradient approximation made simple. *Phys. Rev. Lett.* **77**, 3865–3868 (1996).
69. Anisimov, V. I., Aryasetiawan, F. & Lichtenstein, A. I. First-principles calculations of the electronic structure and spectra of strongly correlated systems: the LDA + U method. *J. Phys. Condens. Matter* **9**, 767–808 (1997).
70. Anisimov, V. I., Zaanen, J. & Andersen, O. K. Band theory and Mott insulators: Hubbard U instead of Stoner I. *Phys. Rev. B* **44**, 943–954 (1991).
71. Jin, J., Chen, J., Wang, H. & Hu, P. Insight into room-temperature catalytic oxidation of NO by CrO₂(110): A DFT study. *Chin. Chem. Lett.* **30**, 618–623 (2019).
72. Janotti, A. & Van De Walle, C. G. Native point defects in ZnO. *Phys. Rev. B* **76**, 165202 (2007).
73. Henkelman, G., Uberuaga, B. P. & Jónsson, H. A climbing image nudged elastic band method for finding saddle points and minimum energy paths. *J. Chem. Phys.* **113**, 9901–9904 (2000).
74. Zhang, R. et al. NO chemisorption on Cu/SSZ-13: a comparative study from infrared spectroscopy and DFT calculations. *ACS Catal.* **4**, 4093–4105 (2014).

Acknowledgements

The research was supported financially by the Division of Chemical Sciences, Geosciences, and Biosciences, Office of Basic Energy Sciences, US Department of Energy (Award No. DE-SC0022273). Spectroscopic and microscopic experiments were performed at the BL7.3.1 at the Advanced Light Source (ALS) and Molecular Foundry at LBNL under contract no. DE-AC02-05CH11231. This research used resources of the National Energy Research Scientific Computing Center, a DOE Office of Science User Facility supported by the Office of Science of the U.S. Department of Energy under contract no. DE-AC02-05CH11231. J.W. and H.Z. acknowledge the support of the U.S. Department of Energy, Office of Science, Office of Basic Energy Sciences (BES), Materials Sciences and Engineering Division under Contract No. DE-AC02-05-CH11231 within the in-situ TEM program (KC22ZH). J.L.C. acknowledges the support of the Ministry of Science and Technology, Taiwan (110-2112-M-213-006). Work at Sandia National Laboratories supported by the U.S. Department of Energy, Office of Science, Basic Energy Sciences (BES) under Field Work Proposal Number 23-024168. Sandia National Laboratories is a multimission laboratory managed and operated by the National Technology & Engineering Solutions of Sandia, LLC, a wholly owned subsidiary of Honeywell International Inc., for the U.S. Department of Energy's National Nuclear Security Administration under contract DE-NA0003525. This paper describes objective technical results and analysis. Any subjective views or opinions that might be expressed

in the paper do not necessarily represent the views of the U.S. Department of Energy or the U.S. Government. D.L. acknowledges the Kwanjeong Study Abroad Scholarship from the KEF (Kwanjeong Educational Foundation) (KEF-2019).

Author contributions

J.S. and S.S. designed the experiments and D.-E.J. designed the DFT calculations. J.Y. synthesized the catalysts and evaluated the catalytic performance, and analyzed the data. L.W. did the DFT calculations. J.W. performed TEM experiments for sample screening, and analyzed the data. F.E.G. and A.F.C. did APXPS experiments and analyzed the data. B.E.M. performed XRF measurements. J.L.C. and L.C.H. performed the XAFS measurements and analyzed the data. D.L. did XRD measurements. X.Z. did XPS experiment. C.W. performed N₂ physisorption measurements. Z.D. contributed to characterization analysis. F.R. and H.B. performed thermodynamic limit analysis. H.Z., M.S., G.A.S., H.L. and D.P. provides suggestions with project design. J.S., S.S., D.-E.J., J.Y., L.W., J.W. and F.E.G. wrote the manuscript, and all the authors contributed to the overall scientific interpretation and edited the manuscript.

Competing interests

The authors declare no competing interests.

Additional information

Supplementary information The online version contains supplementary material available at <https://doi.org/10.1038/s41467-024-44918-8>.

Correspondence and requests for materials should be addressed to De-en Jiang, Seema Singh or Ji Su.

Peer review information Nature Communications thanks Stavros Theofanidis, Nikolay Nesterenko and the other, anonymous, reviewer(s) for their contribution to the peer review of this work. A peer review file is available.

Reprints and permissions information is available at <http://www.nature.com/reprints>

Publisher's note Springer Nature remains neutral with regard to jurisdictional claims in published maps and institutional affiliations.

Open Access This article is licensed under a Creative Commons Attribution 4.0 International License, which permits use, sharing, adaptation, distribution and reproduction in any medium or format, as long as you give appropriate credit to the original author(s) and the source, provide a link to the Creative Commons license, and indicate if changes were made. The images or other third party material in this article are included in the article's Creative Commons license, unless indicated otherwise in a credit line to the material. If material is not included in the article's Creative Commons license and your intended use is not permitted by statutory regulation or exceeds the permitted use, you will need to obtain permission directly from the copyright holder. To view a copy of this license, visit <http://creativecommons.org/licenses/by/4.0/>.

© The Author(s) 2024